

JGR Solid Earth

RESEARCH ARTICLE

10.1029/2021JB023024

Key Points:

- High-resolution mascon trends are estimated directly from 16+ years of GRACE and GRACE-FO Level 1B data
- The new high-resolution global trend product shows improved signal recovery compared to other methods of time variable gravity estimation
- We compare our new trends to mass rates derived from ICESat and ICESat-2 and demonstrate the ability to observe individual glacier systems

Correspondence to:

B. D. Loomis,
bryant.d.loomis@nasa.gov

Citation:

Loomis, B. D., Felikson, D., Sabaka, T. J., & Medley, B. (2021). High-spatial-resolution mass rates from GRACE and GRACE-FO: Global and ice sheet analyses. *Journal of Geophysical Research: Solid Earth*, 126, e2021JB023024. <https://doi.org/10.1029/2021JB023024>

Received 12 AUG 2021
Accepted 19 NOV 2021

High-Spatial-Resolution Mass Rates From GRACE and GRACE-FO: Global and Ice Sheet Analyses

Bryant D. Loomis¹ , Denis Felikson^{1,2} , Terence J. Sabaka¹ , and Brooke Medley¹ 

¹NASA Goddard Space Flight Center, Geodesy and Geophysics Laboratory, Greenbelt, MD, USA, ²Morgan State University, GESTAR II, Baltimore, MD, USA

Abstract GRACE and GRACE-FO gravimetry data are unique in its ability to observe global water mass variability and has frequently been applied for the determination of global mass rates to quantify the impacts of climate change and human activity on global freshwater availability and land ice evolution. However, its relatively coarse spatial resolution of ~300-500 km at monthly intervals precludes its direct use to measure mass changes in smaller drainage basins and individual glacier systems. We present a new global high-resolution mascon product that improves spatial resolution and signal recovery by estimating trends directly from more than 16 years of Level 1B GRACE and GRACE-FO data. We compare this product to independent gravimetry spherical harmonic trend estimates and to ice sheet mass rates derived from ICESat and ICESat-2 laser altimetry. We demonstrate enhanced global signal recovery and improved agreement with ICESat/ICESat-2 and discuss likely causes for the remaining discrepancies between the gravimetry and laser altimetry solutions.

Plain Language Summary The GRACE and GRACE-FO gravimetry missions uniquely observe the global movement of water and ice mass. Measuring the rates of these mass changes has been especially useful for quantifying and understanding the impacts of climate change and human activity on global freshwater availability and land ice evolution. However, the standard monthly data products from these missions are not able to spatially resolve smaller drainage basins and individual glacier systems. We present a new product that significantly enhances the spatial resolution of the mass change rates. This is accomplished by directly estimating the rates from more than 16 years of GRACE and GRACE-FO data. We analyze our new results globally and compare our ice sheet mass rates to those derived from ICESat and ICESat-2 laser altimetry measurements. We demonstrate that our new product: (1) improves the recovery of global mass change rates, (2) is capable of measuring mass rates for individual glacier systems, and (3) is useful for identifying the likely causes for the remaining discrepancies between the gravimetry and laser altimetry solutions.

1. Introduction

The GRACE (2002–2017) and GRACE-FO (GFO; 2018–Present) satellite missions have revolutionized the ability to monitor global and regional mass variability in the hydrosphere, cryosphere, ocean, and solid Earth. As the length of the data record has grown, the quantification of mass trends has been of primary interest for advancing our understanding of changes in land ice and the storage and availability of global freshwater (Jacob et al., 2012; Luthcke et al., 2013; Rodell et al., 2018; Scanlon et al., 2018; Velicogna et al., 2020). The most common approach for computing the mass trends has been to fit a regression model to the monthly data products, where the model parameters at minimum include a bias, trend, and annual sine and cosine. These various efforts to compute mass trends have utilized both the Level 2 spherical harmonics (SH) and higher level products such as regularized mascons (Loomis, Luthcke, & Sabaka; 2019; Save et al., 2016; Watkins et al., 2015) and have been successful at capturing the mass rates at the relatively coarse spatial resolution of ~300–500 km; i.e., the resolution of the monthly products.

More recently, Kvas et al. (2020) developed the GOCO-06S gravity model by estimating regularized regression SH coefficients directly from a combination of GRACE Level 1B data and other satellite data (see Section 2.1), resulting in mass trend estimates with improved spatial resolution and signal recovery beyond those derived from the Level 2 monthly products. Loomis, Richey, et al. (2019) applied the same concept (with GRACE data only), but in lieu of SH, a global set of regularized regression mascons was estimated, with the results also demonstrating significant enhancements to the recovered signal and resolution. Though Loomis, Richey, et al. (2019) did

estimate global mascon trends, the analysis and discussion focused on the High Mountain Asia region and the effort to close the mass trend budget with a combination of geodetic glacier mass balance measurements, groundwater data, and hydrological models.

The work presented here is an extension to Loomis, Richey, et al. (2019), where we present and analyze for the first time the global set of estimated mascon trends, including an updated solution using data from GFO. We make use of the high-quality GOCO-06S spherical harmonic product for comparing and validating our new solution, and leverage this comparison for approximating the uncertainties. Additionally, we compare the GSFC and GOCO-06S GRACE/GFO trend estimates of Greenland Ice Sheet (GrIS) and Antarctic Ice Sheet (AIS) grounded ice to those recently derived from ICESat and ICESat-2 data and presented by Smith et al. (2020). These analyses demonstrate the utility of our new high-resolution trend product and inform an important discussion on the geographic regions where the altimetry-derived mass trend estimates likely need improvement and possible causes of the existing discrepancies.

2. Data and Methods

2.1. GRACE and GRACE-FO

This study compares global trend estimates for several different GRACE/GFO data products. These include mass trends determined from the monthly Level 2 SH provided by the University of Texas Center for Space Research (CSR), the GOCO-06S high-resolution regression SH provided by TU Graz (Kvas et al., 2020), and the monthly and high-resolution regression mascon products developed by NASA GSFC. For the CSR RL06 Level 2 analysis, we consider results with and without the application of DDK5, an anisotropic filter that is commonly used to mitigate the errors at the smaller spatial wavelengths of GRACE Level 2 products (Kusche et al., 2009). The trend maps are derived by fitting a bias, trend, and annual regression model to each SH coefficient up to degree 60. We note that CSR also provides monthly estimates to degree 96, but that produced more unrealistic anomalies in the global trend map than the degree 60 solution. The GOCO-06S product coestimates the static (bias), trend, and annual signals directly from the Level 1B data, where the static portion is estimated to harmonic degree 300 and the trend and annual are estimated to degree 200. The data only actually contribute to the trend and annual terms up to degree 120, while the higher degrees improve the resolution of land/ocean boundaries through the use of regularization. In addition to GRACE data from April 2002 to August 2016, the GOCO-06S solution also incorporates satellite laser ranging (SLR) tracking data, GNSS-derived kinematic orbits of low-Earth orbiter satellites, and GOCE gravity gradiometer data. GOCO-06S is the latest version in a series of GOCO gravity models, and the mass trends are almost entirely determined from GRACE data, except for the lowest degree and order terms for which SLR also contributes. For consistency in the analysis presented here, all trends in the degree 1 (i.e., geocenter) and C_{20} terms are determined from the GFO Technical Note 13 (Sun et al., 2016) and Technical Note 14 (Loomis, Rachlin, & Luthcke, 2019), respectively. When GFO data are included in the trend estimates, the C_{30} values in Technical Note 14 are also applied (Loomis et al., 2020).

The global GSFC monthly mascon product and estimation procedures are described in detail by Loomis, Luthcke and Sabaka (2019) and Luthcke et al. (2013), while the first estimate of high-resolution mascon trends are presented by Loomis, Richey, et al. (2019). The latest GSFC mascon products utilize the microwave interferometer data for GRACE and GFO (i.e., not the GFO laser ranging interferometer) and apply the state-of-the-art geophysical background models in the Level 1B data processing, including the RL06 AOD1B atmosphere and ocean de-aliasing product (Dobslaw et al., 2017). The equations for estimating the full set of regression mascons (bias, trend, annual sine, and cosine per mascon) are developed in Appendix A. In essence, the methodology is the same as that presented by Kvas et al. (2020), except that we build the regularization and least-squares inversion for a global set of 1-arc-degree equal-area mass concentration cells (i.e., mascons) directly from the Level 1B data rather than global SH coefficients. We employ a diagonal regularization matrix, \mathbf{P} (Equations A4 and A5), whose values are determined from the lower resolution regression fits to the monthly mascons (see Appendix A for details). The use of a diagonal regularization matrix for the high-resolution estimation procedure is a notable change from the region-based block-diagonal structure we apply when estimating monthly mascons. This block-diagonal approach applies exponential taper spatial constraints between mascons within the same region (e.g., GrIS), and a recent study by Croteau et al. (2021) demonstrates that this regularization structure is very important for mitigating signal leakage across constraint region boundaries (e.g., from GrIS to the ocean) for monthly 1-arc-degree mascons. However, by incorporating many years of GRACE data in the inversion scheme,

we significantly enhance the spatial data coverage and remove the need for these regional spatial constraints. This conclusion is supported by the small differences that exist in the regression estimates for full regions (e.g., GrIS) between the monthly and high-resolution products (not shown). Note that the GSFC mascon products contain metadata that includes the assigned region for each mascon; e.g., ice sheet, ocean, and land. We also note that we do not present the estimated annual parameters here as that will be the focus of future work, though initial results show similar enhancements to the spatial resolution as observed for the high-resolution mascon trend estimates.

All of the gravimetry mass trend estimates presented below are corrected for glacial isostatic adjustment (GIA), the ongoing viscoelastic response of the solid Earth to the large ice mass losses in the millennia following the last glacial maximum about 20,000 years ago. For the presented global analysis, we use the ICE-6G_D model (R. W. Peltier et al., 2018), while the ice sheet gravimetry analysis applies the same GIA correction as Smith et al. (2020). In the global analysis, we do not restore the ocean surface pressure of the AOD1B product (GAD), as is common for monthly mascon products, and so the presented trends are consistent with the mass change information in the Level 2 GSM SH products with the GIA correction applied. We also note that all presented trends have sought to remove the impact of the largest earthquake coseismic (i.e., step function) events that occurred during the course of the GRACE and GFO missions. GOCO-06S applies an estimation procedure to remove the three largest events: 2004 Sumatra-Andaman, 2010 Maule, and 2011 Tohoku-Oki. Alternatively, GSFC includes a gravity model of the largest coseismic events in the set of background models applied when processing the Level 1B data in order to remove their effect from the inter-satellite ranging data. The GSFC forward model includes the five coseismic events described by Han et al. (2013), which adds the 2007 Bengkulu and 2012 Indian Ocean earthquakes to the list of three given above. For consistency, we also remove the same set of five coseismic events from the CSR SH prior to solving for the global trends. The remaining trends in these regions are largely driven by post-seismic gravity signals (Han et al., 2013).

2.2. Uncertainties

We seek to assign realistic uncertainties to the high-resolution GSFC mascon trend estimates presented here. Globally, the errors are primarily driven by the solution noise, for which the statistics are well-described by the difference of the independent high-resolution trend estimates of GSFC and GOCO-06S (Figure 2a), as these products have unique Level 1B data processing and estimation methods. Given the speckle-like nature of the solution noise, which is largely driven by the higher degree and order terms in the GOCO-06S solution (Figure 1c), we assess this error source by region rather than by individual mascons. This approach avoids both the underestimation of GSFC errors in cases where the speckle-like noise is close to zero, and the overestimation of GSFC errors where it is largest. For each mascon within a given region (e.g., GrIS; land; etc.), we define the solution noise as the standard deviation of the mascon differences within that region: $\sigma_{\text{mascon}} \equiv \sigma_{\text{reg}}$. When reporting the uncertainties for a region or subregion, as in Tables 1 and 2, we compute the standard error: $\sigma_{\text{subreg}} = \sigma_{\text{reg}} / \sqrt{n_{\text{subreg}}}$, where n_{subreg} is the number of mascons in a given subregion, and the subregion is any set of mascons contained by the full region where the mascon difference statistics have been used to compute σ_{reg} . The use of different regions when defining the uncertainties is necessary because their magnitudes are correlated with the signal magnitude (Loomis, Luthcke, & Sabaka, 2019). In Table 1, we define the region as the lower elevation (<2000 m) portion of the corresponding ice sheet, as that is where the glacier systems are located, and the subregion is described by the mascons listed in the first column (e.g., $\sigma_{\text{Jakobshavn}} = \sigma_{\text{GrIS}<2000\text{m}} / \sqrt{n_{\text{Jakobshavn}}}$). In Table 2, each region is defined by the ice sheet identified in the first column (e.g., $\sigma_{\text{GrIS}} = \sigma_{\text{GrIS}} / \sqrt{n_{\text{GrIS}}}$). In some regions, including the ice sheets investigated here, the GIA errors are also significant and must be accounted for (see Appendix B). The total uncertainties for the GSFC trend estimates are then defined as twice (i.e., $2 - \sigma$) the root sum square (RSS) of the solution errors and GIA errors.

Additionally, previous work in our group has focused on the assessment of solution bias (or leakage bias) induced by the regularization applied in the estimation of mascons (Loomis, Luthcke, & Sabaka, 2019; Loomis, Richey, et al., 2019). To briefly summarize, if we neglect noise, the solution bias for a regularized solution is equal to $(\mathbf{R} - \mathbf{I})\mathbf{x}$, where \mathbf{R} is the resolution operator, \mathbf{I} is the identity matrix, and \mathbf{x} is the (unknown) vector of true mascons. The resolution matrix is the linear operator through which the true, underlying state is filtered into the least-squares estimate. Its departure from the identity operator, often due to regularization, is one of two typical sources of error in least-squares estimation that results in biased estimates. The other is assumed Gaussian system noise, which leads to estimation variance. A useful application of the resolution operator is to compute the

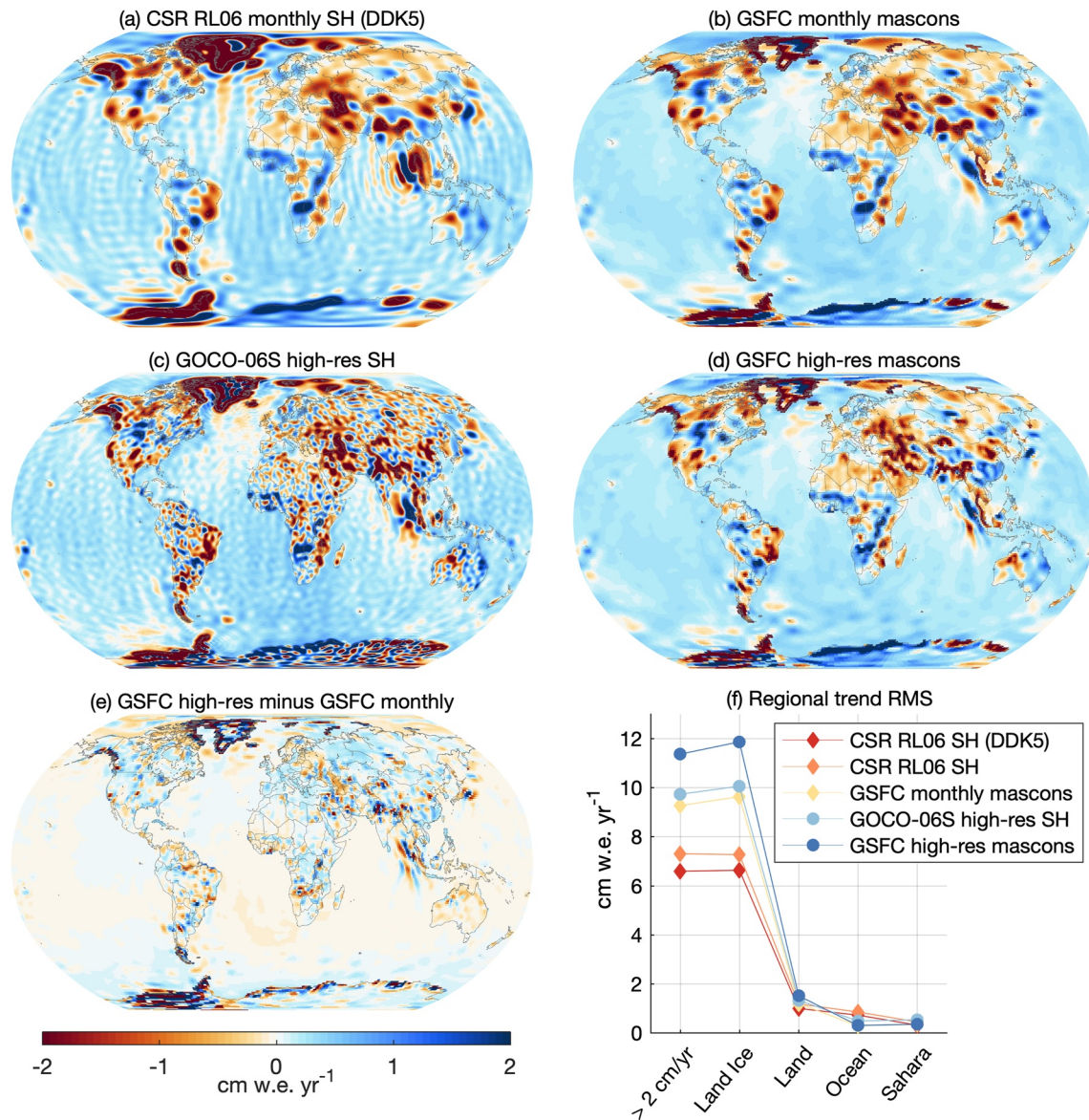


Figure 1. GRACE global mass trends for April 2002 to August 2016: (a) CSR RL06 Level 2 monthly spherical harmonics (SH) with DDK5 filter applied; (b) GSFC monthly mascon product; (c) GOCO-06S high-resolution SH; (d) GSFC high-resolution mascon product; (e) Difference between the GSFC high-resolution mascons and GSFC monthly; (f) Regional comparison of the RMS of trend values for the various solutions where the SH solutions have been evaluated at the mascon locations. The first region in (f) is the subset of global mascons for which the evaluated GOCO-06S trends' magnitudes exceed 2 cm w.e. per year. The land ice region includes mascons covering the Greenland and Antarctic Ice Sheets and Gulf of Alaska. The color scale has been set at ± 2 cm w.e. yr^{-1} for all maps to match Figure 1 in Rodell et al. (2018).

GRACE/GFO mascon solution bias under the assumption that some independent data set is equal to the truth as was done by Loomis, Richey, et al. (2019). For the analysis presented in Tables 1 and 2, we provide the regional bias estimates by applying the GSFC high-resolution trend resolution operator in the above equation with the mascon-averaged ICESat/ICESat-2 estimates (see Section 2.3) to define the truth vector, \mathbf{x} . This is essentially the same approach followed by Loomis, Richey, et al. (2019) for building confidence intervals to compare GRACE mascons and independent mass trend estimates in High Mountain Asia. Under the assumption that the ICESat/-2 solution is the truth, the estimated GSFC leakage biases would be removed from the GSFC estimates before comparing to the ICESat/-2 estimate.

It is worth clarifying exactly what we mean by the term “leakage,” as it is an important part of the discussion regarding the enhanced spatial resolution of the GSFC high-resolution trends. In GRACE studies, leakage refers

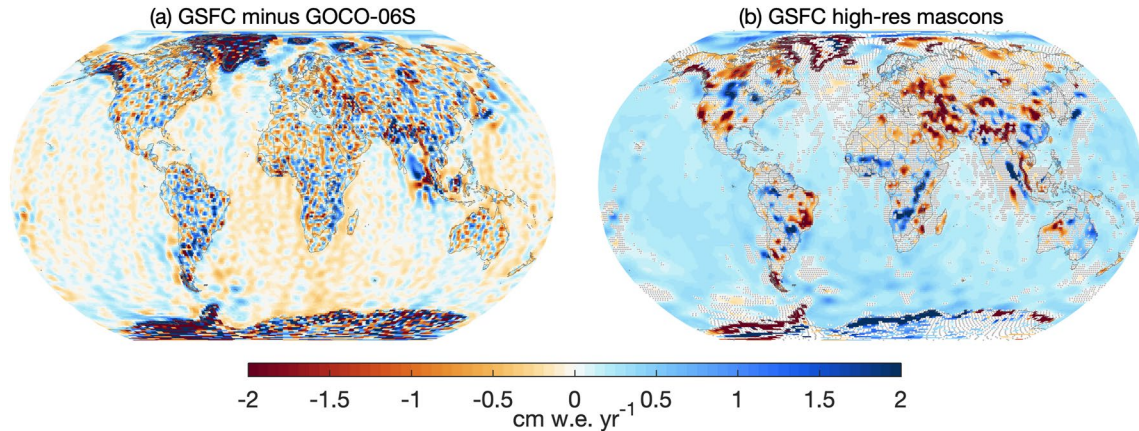


Figure 2. Mascon uncertainty and significance: (a) Difference between the GSFC high-resolution mascons (Figure 1d) and GOCO-06S (Figure 1c); (b) GSFC high-resolution mascons, except mascons where the magnitude of Figure 1d is less than the magnitude of Figure 2a are colored in gray.

to errors in the proper geolocation of the true signal source. With spherical harmonics, this is associated with the limited expansion of the coefficients and the commonly applied filters that generally result in signal smoothing. For regularized mascon estimation, this unwanted movement and/or smoothing of the true signal can be rigorously assessed with the resolution operator as described above. We term this type of leakage error “inter-mascon leakage,” as this describes the movement of signals between mascons. A different type of leakage error, which we will call “intra-mascon leakage,” is simply due to the fact that each individual 1-arc-degree mascon is assigned

Table 1

Glacier System and Regional Trends for Various Solutions: CSR RL06 Level 2 Monthly Spherical Harmonics (SH) With and Without the DDK5 Filter Applied, GSFC Monthly Mascons, GOCO-06S High-Resolution SH, GSFC High-Resolution Mascons, and ICESat-2 Values From (Smith et al., 2020) Averaged Into the GSFC Mascon Cells. The GSFC Leakage Bias Estimates are Determined With the GSFC Resolution Operator and the ICESat-2 Mascons. All Units are Gt yr⁻¹

Glacier system / region	CSR monthly	CSR monthly	GSFC monthly	GOCO-06S high-res	GSFC high-res	GSFC bias	ICESat-2 mascons
(GSFC mascon numbers)	SH	SH DDK5	mascons	SH	mascons		
Jakobshavn (73 77 78)	-8.3	-6.2	-14.9	-20.2	-24.4 ± 4.4	4.6	-26.0
Kangerdlugssuaq (79)	-2.4	-1.8	-4.2	-5.3	-6.7 ± 2.5	1.8	-9.2
Helheim (90)	-2.1	-2.2	-4.8	-4.2	-4.5 ± 2.5	1.6	-9.1
Northwest Coast (47 51 54 59)	-11.1	-8.9	-22.5	-20.6	-30.1 ± 5.0	4.5	-32.0
Pine Island (685 686 687 688 752 753 754)	-28.1	-25.5	-33.9	-44.2	-55.0 ± 3.1	-0.8	-54.4
Thwaites (684 749 750 751 816 817)	-27.6	-24.8	-32.0	-32.2	-40.0 ± 2.8	2.3	-39.9
Haynes/Pope/Smith/Kohler (681 682 683 748)	-14.5	-14.1	-16.5	-22.2	-25.7 ± 2.3	0.0	-32.1
Totten (234 235 270 271)	-4.0	-3.0	-5.4	-9.8	-9.1 ± 2.3	0.6	-12.1
Inland of Kamb Ice Stream (1063 1064 1065)	2.4	2.6	3.4	6.7	10.2 ± 2.1	-2.9	12.4

Table 2

GSFC GRACE/GFO and Smith et al. (2020) ICESat/ICESat-2 Ice Sheet Regional Mass Trend Comparison. The Same GIA Correction Applied by Smith et al. (2020) Has Been Applied for GRACE/GFO. The GSFC High-Resolution Mascon Uncertainties are the RSS of the Solution Error (Figure 2a) and GIA Error. The GSFC Leakage Bias Estimates are Determined With the GSFC Resolution Operator and the Smith et al. (2020) Solution Averaged Into Mascons. All Units are $Gt\ yr^{-1}$

Ice sheet	Full mascon region ^a			Grounded ice mascon region ^b			
	GSFC high-res	Bias	GIA	GSFC high-res	Bias	GIA	ICESat/-2
GrIS	-282 ± 35	5	2 ± 11	-209 ± 29^c	-2	0 ± 8	-200 ± 12
WAIS	-148 ± 27^c	3	32 ± 14	-143 ± 26	4	30 ± 13	-169 ± 10
AP	-34 ± 10^c	-1	4 ± 2	-19 ± 6	1	3 ± 2	-39 ± 5
EAIS	69 ± 29^c	-2	20 ± 25	69 ± 29	-4	18 ± 26	90 ± 21
AIS	-113 ± 39^c	1	56 ± 26	-93 ± 38	1	51 ± 26	-118 ± 24

^aMatches the GSFC mascon definitions; includes peripheral glaciers and ice caps for GrIS. ^bSubset of GSFC mascons with at least 30% ICESat/ICESat-2 data coverage. ^cRecommended GRACE/GFO regional estimate for comparing with ICESat/ICESat-2 (see text).

a single value and by definition cannot distinguish the source of the signal within a given mascon. For instance, a single GSFC mascon that is designated as land in the mascon metadata and regularization, but overlaps the coast, will “leak” land signal into the portion of the ocean overlaid by the mascon (note that the GSFC product metadata identifies the designated region of each mascon; e.g., land, ocean, GrIS, etc.). Various approaches exist to address intra-mascon leakage, but the GSFC 1-arc-degree grid already significantly over-samples the fundamental monthly spatial resolution of GRACE/GFO, meaning that the role of intra-mascon leakage in the GSFC solution is insignificant relative to inter-mascon leakage for monthly estimates. The work presented in this manuscript suggests that enhancing the spatial resolution of our mascons beyond 1-arc-degree may be warranted for the high-resolution trends, and this is a topic to be further investigated. References to leakage below refer to inter-mascon leakage, which is what is most often meant in the GRACE/GFO literature when discussing this important error source.

2.3. ICESat and ICESat-2

The ICESat (2003–2009) and ICESat-2 (2018–Present) laser altimetry missions (collectively referred to as ICESat/-2 throughout) determine ice sheet topography and height changes to a much higher spatial resolution than is achievable for mass change estimates from spaceborne gravimetry. Height changes of grounded ice are the result of both variability in ice thickness and solid Earth processes. Total ice thickness changes are the combination of surface mass balance, ice dynamics, and changes in firn density (Csatho et al., 2014), while the solid Earth heights are impacted by GIA and the elastic response to changing surface mass loads (Smith et al., 2020). This same set of ice and solid Earth processes also cause variability in the total mass that is captured by the gravimetry missions, with the exception of firn density changes which only affect the height. A primary goal of both the gravimetry and laser altimetry missions is to quantify the evolution of grounded ice mass over the ice sheets, as it directly impacts global mean sea level and accounts for about one-third of sea level rise during the GRACE era (Loomis, Luthcke, & Sabaka, 2019). The recent study by Smith et al. (2020) presents a new estimate of ice mass rates over GrIS and AIS on a 5 km grid. This new product was derived from ICESat/-2 data in conjunction with state-of-the-art firn density and solid Earth corrections that are required to convert from the observed height trends to trends of ice mass. After accounting for the significant difference in spatial resolution, the new ICESat/-2 mass trend estimates can be directly compared to those determined with GRACE/GFO. This is achieved by taking the average of the 5 km gridded ICESat/-2 trend estimates within each GSFC 1-arc-degree mascon cell ($\sim 111 \times 111$ km).

3. Results and Discussion

3.1. Global GRACE-Only Trends

Figures 1a–1d present four different global mass trend estimates derived from GRACE data over the span from April 2002 to August 2016: CSR RL06 SH with DDK5 filter applied, GSFC monthly mascons, GOCO-06S SH, and GSFC high-resolution mascons, respectively. Visual inspection of these figures shows speckled noise in both SH solutions, which is due to the increased errors at higher SH degrees and orders (Loomis et al., 2019). The CSR trend exhibits the distinctive north-south striping that is caused by temporal aliasing and limited east-west sensitivity of the along-track inter-satellite ranging measurements (Elsaka et al., 2014), while this non-geophysical feature is far less prominent for GOCO-06S. The reduction of this systematic error in GOCO-06S is likely due to a combination of the applied regularization and the increased spatiotemporal resolution afforded by using 14+ years of data in the least-squares inversion. We also note that the reduced degree and order expansion of the CSR SH causes ringing artifacts in the vicinity of the largest signals, which is the well-known Gibbs phenomenon. Alternatively, the regularization applied to both mascon products, significantly mitigates the speckled noise and north-south striping errors and appears to be free of Gibbs ringing. These global trend maps also reveal notable improvements in signal recovery and spatial resolution for the high-resolution products (Figures 1c and 1d) as compared to the monthly products (Figures 1a and 1b). This enhanced signal recovery is especially clear in Figure 1e that plots the difference between the GSFC high-resolution and monthly trends.

To quantify these improvements, Figure 1f reports the root mean square (RMS) of the same four solutions for different regions, with the unsmoothed CSR SH solution also included in the comparison. Aside from major earthquake events, the geophysical processes that cause the largest mass trends are the variability of land ice and terrestrial water storage occurring over non-arid land regions. Conversely, we expect mostly small trend magnitudes over the ocean and arid regions like the Sahara desert. For the results shown in Figure 1f, the SH products are evaluated at the GSFC mascon locations. The first group of mascons analyzed is the subset of all mascons for which the evaluated GOCO-06S trends have a magnitude greater than $2 \text{ cm w.e. yr}^{-1}$ (1591 mascons). The other regions are land ice, consisting of GrIS, AIS, and Gulf of Alaska (1293 mascons), all other land (11 603), ocean (27 809), and the Sahara Desert (596). The GSFC high-resolution product has the largest signal RMS for the first three considered regions where the largest trends are expected. For the ocean and Sahara, the two GSFC products have essentially the same RMS, resulting in the smallest value of all solutions for the ocean and the second smallest for the Sahara. This analysis demonstrates that the GSFC high-resolution product has the largest signal-to-noise ratio of the different trend estimates considered here. This signal enhancement relative to the monthly mascons results from the ability to relax the applied regularization, which is enabled by the use of many years of data in the inversion.

Figure 2a presents the differences between the GSFC high-resolution and GOCO-06S estimates, while Figure 2a is the same GSFC high-resolution solution shown in Figure 1d, except mascons with a trend magnitude less than the differences shown in Figure 2a have been grayed out. The remaining 71% of global mascons are determined to be significant with the assumption that the difference between these independent solutions is a good approximation of error.

3.2. Global GRACE/GFO Trends

In Figure 3a, we present our most up-to-date estimate of global mass trends by adding GFO data from June 2018 to September 2020 to the GRACE data applied in Figure 1. Note that we have intentionally excluded the end-of-mission GRACE data due to the loss of functionality of an accelerometer after August 2016. While both late-GRACE and GFO gravity estimates rely on a transplant accelerometer Level 1B data product, the negative impact on the gravity estimates appears to be far greater for GRACE (Landerer et al., 2020), presumably due to the lower altitude and corresponding increase in drag forcing. Figure 3b shows the difference between this updated solution and the GRACE-only estimate presented in Figure 1d. These differences highlight the fact that many of the trends observed by GRACE/GFO are not stationary, but rather are influenced by interannual variability in various mass change signals. Analysis of these changes in the global trends over time is beyond the intended scope of this paper. However, we do hope that this new product will aid in improving our understanding of the important global freshwater trend analyses discussed in previous studies, such as Rodell et al. (2018) and Scanlon et al. (2018), and that the enhanced spatial resolution will facilitate the discovery and investigation of other important natural,

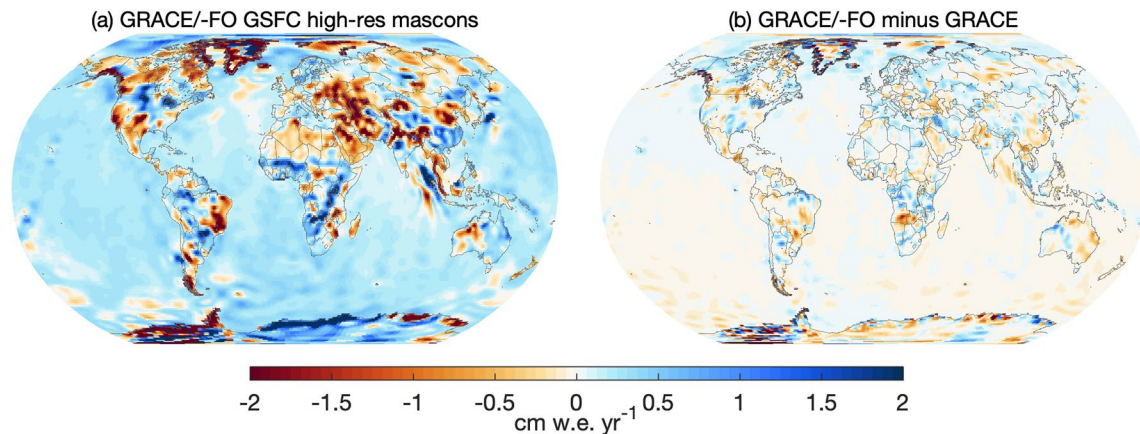


Figure 3. Updated mass trend estimates with the inclusion of GRACE-FO data: (a) GSFC high-resolution mascon product using GRACE data for April 2002 to August 2016 and GRACE-FO data for June 2018 to September 2020 and (b) The change in trends due to the inclusion of GRACE-FO data; i.e., the difference between Figures 1d and 3a.

climate change, and human impacts on global water storage changes not previously observed by the GRACE missions. We also anticipate that computing separate high-resolution trend solutions over different spans will provide important insights on the observed mass rates and their persistence or variability.

3.3. Ice Sheet Trends From GRACE/GFO and ICESat/ICESat-2

We now focus the discussion on the mass rates observed for GrIS and AIS and the comparison between the GRACE/GFO estimates and those derived with ICESat/-2. For the sake of space, we have omitted the CSR monthly spherical harmonic solution from the spatial comparison in Figure 4, noting that the substantial leakage

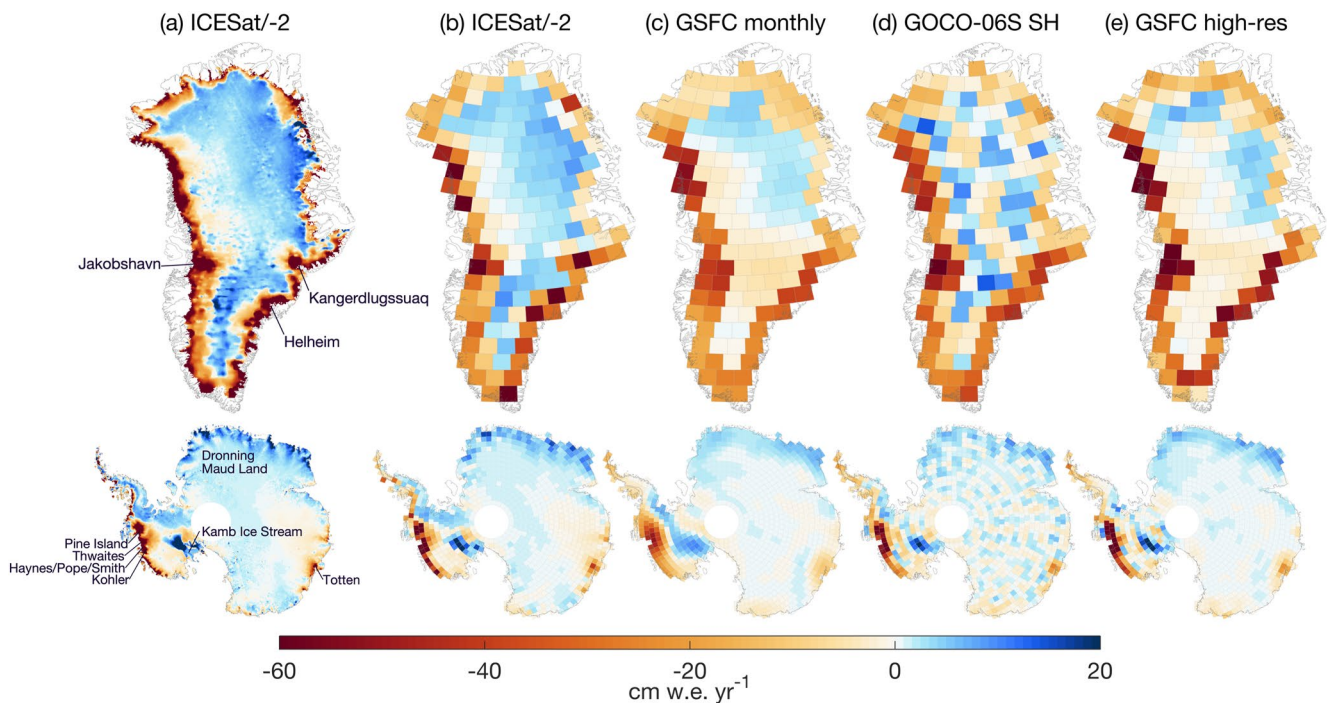


Figure 4. Mass trend comparisons for the Greenland and Antarctic Ice Sheets: (a) ICESat/ICESat-2 solution of Smith et al. (2020); (b) ICESat/ICESat-2 solution averaged into GSFC mascon cells; (c) GSFC monthly mascon trends; (d) GOCO-06S spherical harmonic trend computed at GSFC mascon locations; (e) GSFC high-resolution mascon trends. (b) through (e) show mascons with at least 30% of ICESat/ICESat-2 data coverage and is not the full subset of ice sheet mascons defined in the GSFC products.

clearly visible in Figure 1a leads to poor agreement with ICESat/-2 compared to the other solutions. Figure 4a presents the 5 km by 5 km gridded ICESat/-2 mass trends estimated by Smith et al. (2020), while Figure 4b shows the same trends averaged into the GSFC mascon cells. Figures 4b–4e show the subset of ice sheet mascons with at least 30% of spatial data coverage for the Smith et al. (2020) ICESat/-2 data product, which is not the full subset of ice sheet mascons defined in the GSFC GRACE/GFO products. This was done in order to limit the comparison to the mascons where the ice sheet mass rates determined with ICESat/-2 are the primary signal captured by GRACE/GFO and to exclude the subset of GSFC mascons with significant overlap with the ocean, ice shelves, and peripheral glaciers and ice caps (GIC). GSFC mascons that overlap both land and ocean (or ice shelves) are generally defined as land in order to best capture the larger monthly mass change signals over the land regions while mitigating signal leakage from the land to the ocean. As discussed in Section 2.1, these regional definitions are applied in the monthly regularization but not in the estimation of the high-resolution trends. The percent discrepancy between mascons with at least 30% data coverage and the full set of regional GRACE/GFO mascons is larger for GrIS (149 out of 198; 25% difference) than for AIS (975 out of 1053; 7% difference). As discussed below, this selection of 30% data coverage requirement has a notable impact on the reported GRACE/GFO regional grounded ice mass loss rates for GrIS but a much smaller impact for AIS. For clarity, we refer to the grounded ice region in Greenland as GrIS and the full region as GrIS+GIC.

Consistent with the global analyses, the maps of the ice sheet trends (Figure 4) and rates of localized mass loss (Table 1) reveal enhanced signal recovery and spatial resolution for the high-resolution products as compared to the monthly. The GOCO-06S solution again shows some non-geophysical speckled errors not present in the high-resolution GSFC trends, especially over large portions of East AIS and the high elevation interior of GrIS (also note that GOCO-06S does not include any GFO data). In GrIS, the high-resolution products demonstrate a clear enhancement over both the GSFC monthly mascons and the GOCO-06S SH solutions of the large dynamic loss rates in the vicinity of the Kangerdlugssuaq, Jakobshavn, and Helheim glaciers, and the collection of other marine-terminating glaciers concentrated along the northwest coast (Mouginot et al., 2019). In West AIS, we observe a similar enhancement of the large well-documented mass loss rates in Amundsen Sea Embayment that are driven by dynamic ice mass losses in the Pine Island, Thwaites, Haynes, Pope, Smith, and Kohler Glaciers (Mouginot et al., 2014; Sutterley et al., 2014; Rignot et al., 2019). We also observe a slight sharpening of the mass loss signals in Wilkes Land for both the GOCO-06S and GSFC high-resolution mascons as compared to the monthly mascons, especially for Totten Glacier (Li et al., 2015). The high-resolution solutions also increase the magnitude and resolution of the most notable mass gains in AIS, including those due to positive surface mass balance anomalies in East AIS along the coast of Dronning Maud Land and the dynamic thickening occurring in West AIS just inland from the Kamb Ice Stream (Joughin et al., 2002; Zwally et al., 2015). The GSFC high-resolution mascons provide the best agreement with the ICESat/-2 estimates for most of the localized regions listed in Table 1, with some demonstrating substantial improvements. We also note that accounting for the GSFC bias estimates improves the agreement with ICESat/-2 for many of the listed regions. In summary, these results lead us to conclude that the GSFC high-resolution product is capable of observing mass rates of individual glacier systems.

By examining several key statistics of the mass trends by ice sheet region, we demonstrate that the GSFC high-resolution trends are comparable or better than the other solutions (Figure 5). These statistics include the signal RMS of GRACE/GFO as compared to ICESat/-2, the RMS difference between ICESat/-2 and GRACE/GFO, and the correlation coefficient between ICESat/-2 and GRACE/GFO. Note that we have excluded the easternmost mascon at the southern tip of GrIS as its ICESat/-2 estimate is an extreme (more than $10 - \sigma$) outlier compared to all GRACE trend solutions and significantly skews all of the statistical metrics presented here (by comparison the rest of the GrIS mascons have zero $4 - \sigma$ outliers for GSFC and two $4 - \sigma$ outliers for GOCO-06S). The GSFC high-resolution trends have the largest signal RMS of all gravimetry solutions for GrIS, West AIS, and the Antarctic Peninsula. Comparing the GOCO-06S and GSFC high-resolution solutions, we observe similar performance in terms of the RMS differences and correlation coefficients with ICESat/-2, while the GSFC high-resolution product out-performs the monthly estimates on all metrics. The improved correlation coefficient for the GSFC high-resolution solution over East AIS is notable, given the challenges in accurately recovering the small mass rates over this very large region.

Next, we present the GSFC high-resolution mascon GRACE/GFO and ICESat/-2 estimates of regional ice sheet trends in Table 2. All provided trends have been corrected for GIA (see Appendix B) with the GIA corrections applied to GRACE/GFO listed in the table. The regional mass trend estimates reported by Smith et al. (2020) are

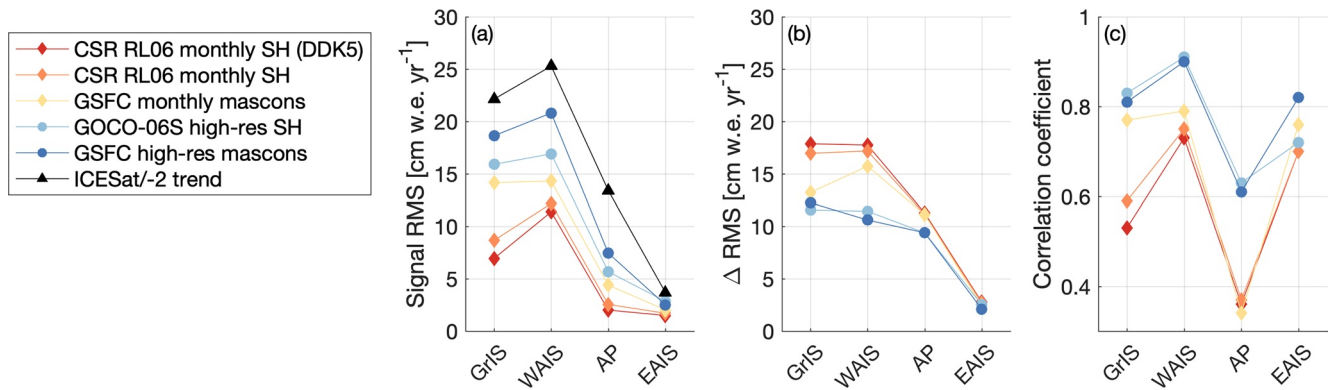


Figure 5. Statistical comparisons between ICESat/ICESat-2 mascon trends in Figure 4b and various GRACE/GRACE-FO solutions for the Greenland Ice Sheet (GrIS), the West Antarctic Ice Sheet (WAIS), the Antarctic Peninsula Ice Sheet (AP), and the East Antarctic Ice Sheet (EAIS): (a) Root-mean-square of the trend values; (b) Root-mean-square of the difference between the ICESat/ICESat-2 and GRACE/GRACE-FO trend solutions; (c) Correlation coefficients between the ICESat/-2 and GRACE trend solutions. The GOCO-06S product uses GRACE data from April 2002 to August 2016. The CSR and GSFC trend estimates use GRACE data from the same span plus GRACE-FO data from June 2018 to September 2020.

also shown. We find excellent agreement between the GRACE/GFO and ICESat/-2 trends for the GrIS grounded ice sheet region ($-209 \pm 29 \text{ Gt yr}^{-1}$ and $-200 \pm 12 \text{ Gt yr}^{-1}$, respectively; Table 2). The small leakage bias values reported in Table 2 demonstrate that the amount of signal leakage from the grounded ice region into the surrounding mascons that make up the rest of the full GrIS+GIC region is not a significant contributor to the differences between the full and grounded ice regions. The difference between the full GrIS+GIC region and the GrIS grounded ice region for the GSFC solution is -73 Gt yr^{-1} , providing a direct GRACE/GFO estimate of peripheral GIC mass losses (the GOCO-06S value is -70 Gt yr^{-1}). However, this value is notably larger than previously published estimates that range from -36 to -41 Gt yr^{-1} , with reported uncertainties of $\sim 16 \text{ Gt yr}^{-1}$ (Bolch et al., 2013; Gardner et al., 2013; Colgan et al., 2015; Noël et al., 2017). The GSFC high-resolution full GrIS+GIC trend of $-282 \pm 35 \text{ Gt yr}^{-1}$ does not fully reconcile with the sum of the ICESat/-2 grounded ice and published peripheral ice estimates, which would be about $-240 \pm 20 \text{ Gt yr}^{-1}$ if we add and RSS the estimates and uncertainties, respectively. Here, we acknowledge that defining the GrIS grounded ice region as the subset of mascons with at least 30% ICESat/-2 data coverage is a somewhat arbitrary choice that seeks to capture the majority of the grounded ice signal while minimizing the contribution of the peripheral ice changes. If we modify the grounded ice definition to require data coverages of 10% and 5%, the GSFC high-resolution GrIS grounded ice estimates become -223 and -244 Gt yr^{-1} , respectively, which correspond to peripheral GIC mass rates of -59 and -38 Gt yr^{-1} . To summarize, GRACE/GFO reports either larger GrIS grounded ice losses than Smith et al. (2020), larger peripheral GIC losses than the noted publications or somewhat larger losses for both, depending on how the partitioning between GrIS and peripheral GIC is done. While our -73 Gt yr^{-1} estimate of the peripheral GIC mass loss rate is likely a bit large due to the inability of the 1-arc-degree mascons to perfectly define and separate the GrIS and peripheral GIS regions, the acceleration in negative surface mass balance rates shown by Noël et al. (2017) leading up to its final data point of 2015 suggests that the updated rate for 2003–2020 could very likely be larger than the previously published range of estimates.

In contrast to the GrIS analysis, for AIS, we propose that it is more appropriate to compare the ICESat/-2 regional estimates with the full GSFC high-resolution GRACE/GFO regional estimates listed in the first column of Table 2. However, we also provide the grounded ice trends following the same 30% data coverage definition for completeness and consistency with the GrIS analysis. As discussed above, it is well-known that there are significant mass changes outside of the GrIS grounded ice region studied by Smith et al. (2020) that influence the gravimetry mass change estimates, but that is not the case for AIS. The mascons along the periphery of AIS with less than 30% data coverage primarily overlap with ocean and ice shelves, so the differences between the full region and grounded ice regions for the GRACE/GFO AIS estimates are primarily due to the inability of the 1-arc-degree mascons to perfectly represent the grounded ice region (see discussion of intra-mascon leakage in Section 2.2). In other words, the removal of mascons with less than 30% data coverage removes true mass change signal associated with the ice sheet. For the full AIS region, we report good agreement between the two measurement techniques, with values of $-113 \pm 39 \text{ Gt yr}^{-1}$ and $-118 \pm 24 \text{ Gt yr}^{-1}$ for GRACE/GFO and ICESat/-2,

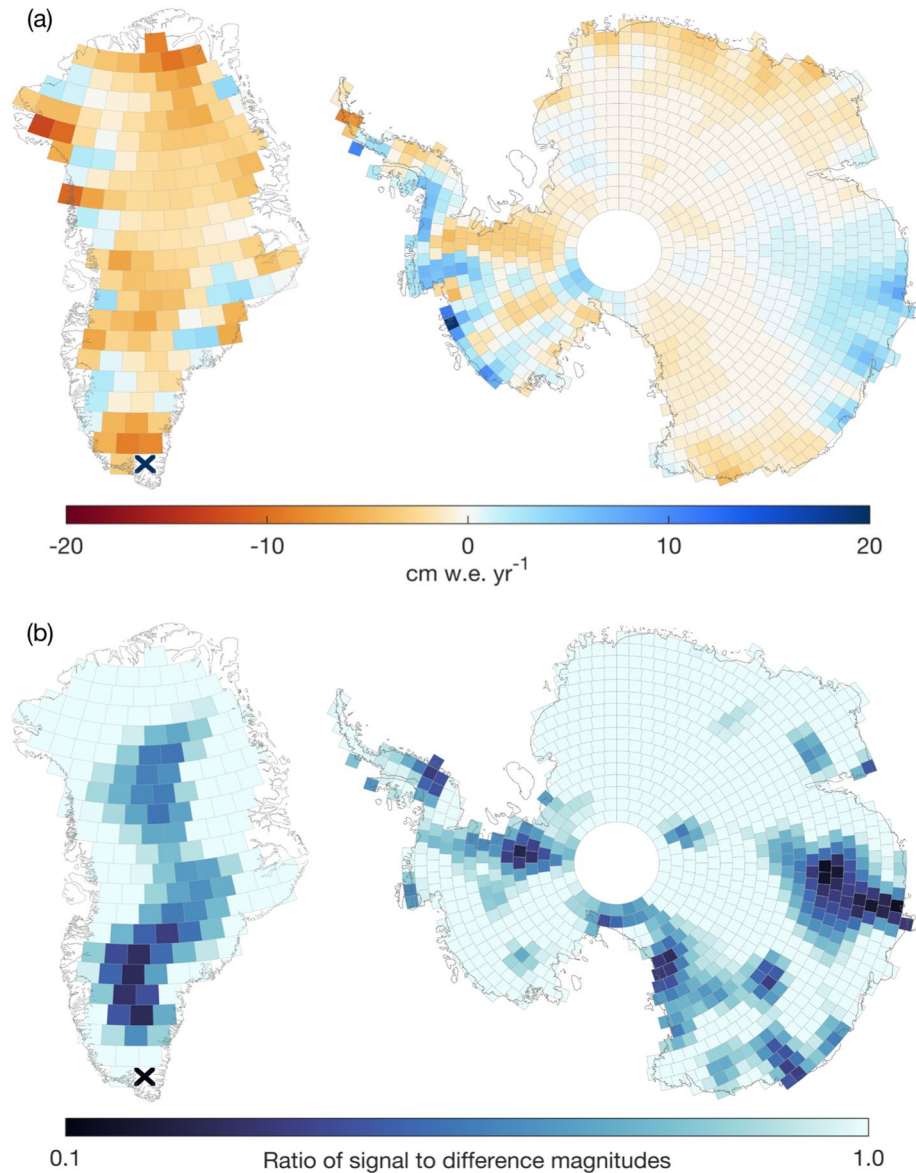


Figure 6. Discrepancies between GRACE/GFO and ICESat-2: (a) Difference between the GRACE/GFO GSFC high-resolution trends and ICESat-2 trends (Figure 4c minus Figure 4b). The results have been lightly smoothed at 100 km to highlight the coherent signal differences rather than the fundamental difference in spatial resolution. The dark blue “X” indicates that the extreme outlier GrIS mascon discussed in Section 3.3 saturates the color scale in the positive direction. (b) Ratio of the GRACE/GFO signal (Figure 4e) to the differences (Figure 6a), again with 100 km smoothing. A log color scale is used to better highlight regions of good and poor signal-to-noise: The lightest color indicates mascons where the magnitude of the signal exceeds the difference magnitude (>1.0) while darker colors indicate the opposite (<1.0). The “X” indicates that the extreme outlier mascon saturates the color scale in the direction of poor signal-to-noise.

respectively. The ICESat-2-derived trends report larger mass increases in East AIS while showing larger losses in West AIS, but when accounting for uncertainties, the GRACE/GFO and ICESat-2 estimates agree for all AIS regions. We note that our computed uncertainties for GIA alone exceed the total uncertainties reported by Smith et al. (2020) for East, West, and the full AIS, suggesting that their assessment of GIA uncertainties might be optimistic. As is observed for GrIS, the leakage bias estimates for AIS, WAIS, AP, and EAIS are also small, indicating that little signal leakage exists between these ice sheet regions.

The differences between the mass change rates derived from GRACE/GFO and ICESat-2 (Figure 6a) allow us to postulate source attribution to the discrepancies for each ice sheet. The maps in Figure 6a indicate the additional

hypothetical correction one would apply to ICESat-2 to perfectly match the GRACE/GFO solution, which we assume are largely driven by errors in the firn air content (FAC) correction, although we note that is an oversimplification. The signal is clear across most of the GrIS; i.e., GRACE/GFO exhibits higher mass loss than ICESat-2 (Figure 6a), suggesting the rates of mass change from ICESat-2 are more positive than GRACE/GFO. The GrIS FAC correction from Smith et al. (2020) (their Figure S4) was predominantly positive, upward of several cm per year, which is indicative of a large loss in FAC. Based on Figure 6a, we find that the modeled loss of FAC over the ICESat-2 interval is likely too large, generating a FAC correction that is too positive. The excess FAC loss could be attributable to several factors, including (1) too much melt, which rapidly removes air from the firn column, (2) unrealistic trends in air temperature and/or snowfall or modeled densification sensitivity to those fluctuations, and (3) underestimation of the surface and near-surface density. Near the GrIS periphery, where mass loss is occurring largely in the ablation zone, there is very little FAC and thus GRACE/GFO and ICESat-2 are in general agreement. This can be seen in the ratio of the mass change signal magnitude to the magnitude of the differences between the GRACE/GFO and ICESat-2 signals (Figure 6b). The interior of the GrIS shows a low ratio of the signal to the differences (<1.0), indicating that the noise has larger magnitude than the signal in this region. On the other hand, this ratio is high (>1.0) around the periphery of the GrIS, indicating that the signal is dominated by ice mass loss rather than by discrepancies between the two measurements caused by the FAC correction, and both ICESat-2 and GRACE/GFO are essentially direct observables of that mass change. For the AIS, Figure 6a reveals synoptic-scale deviations between the two solutions, which vary in sign by location. Specifically, rates of mass change from ICESat-2 are too positive over large portions of Dronning Maud Land, East Antarctic plateau, and portions of eastern WAIS, whereas central and Western WAIS along with Wilkes Land in EAIS are likely too negative. A comparison of Figure 6a and the FAC correction from Smith et al. (2020) (their Figure S5) supports our theory that much of the residual between the GRACE/GFO and ICESat-2 solutions is linked to the FAC correction as the two are remarkably similar. Interestingly, our results suggest the FAC correction applied in Smith et al. (2020) was not large enough, requiring amplification in magnitude, irrespective of the sign, to come into agreement with the GRACE/GFO solution. Because the AIS is largely dry (i.e., free from melt), we hypothesize that the majority of this signal stems from (1) overestimated surface density and (2) underestimated trends in snow accumulation or temperature to a lesser extent. Ultimately, it is challenging to disentangle whether error in the FAC correction comes from the atmospheric forcing (i.e., MERRA-2) or errors in the firn densification model. Future work that directly compares observed height change (rather than a height change corrected for FAC processes), the FAC correction, and GRACE/GFO in conjunction with sensitivity runs of the firn densification model should help shed light on attribution of error sources for both GrIS and AIS. Lastly, the large anomaly identified in the southern tip of the ICESat-2 GrIS solution may have resulted from the sparseness of crossovers in that region, and we are not currently confident in establishing the primary cause (note that this mascon identified with an "X" in Figure 6). Possible contributors include poorly resolved height change measurements, FAC modeling errors, and interpolation and/or aliasing artifacts.

4. Conclusions

We presented a new global high-resolution trend mascon product estimated directly from GRACE Level 1B data that improves the signal recovery and advances the spatial resolution as compared to global trends derived from monthly products. The aim is to provide the scientific community with new information to aid in assessing the natural, climate change, and human impacts on changes in global water storage and land ice. We presented analysis of regional RMS values as validation that our new product improves signal recovery and reduces noise relative to monthly SH, monthly mascons, and the high-quality GOCO-06S high-resolution SH product. We also estimated high-resolution mascon trends that include about two years of GRACE-FO data and quantified the impact by comparing to trends derived solely from GRACE data. With a more focused analysis over the ice sheets, we again observed a clear enhancement in signal recovery for the high-resolution products over those determined from monthly estimates. Again comparing GSFC and GOCO-06S, we reported that the GSFC solution has a higher signal RMS for GrIS, West AIS, and the Antarctic Peninsula, while the other considered metrics (RMS difference and correlation coefficient to ICESat/ICESat-2) showed similar performance between the two products. For future work, we plan to periodically update our high-resolution mascon trends and investigate global trend differences when applying our estimation methods over different spans of GRACE and GRACE-FO data. We speculate that the enhanced precision of the laser ranging interferometer onboard GRACE-FO and a longer data record may further enhance the spatial resolution of our trend estimates than is possible with the

microwave interferometer employed by GRACE (also the primary ranging instrument on GRACE-FO). We also plan to analyze and release the high-resolution annual terms as well as explore the estimation of other temporal functions (e.g., acceleration).

By providing more localized estimates of mass change around the ice sheets, the GSFC high-resolution mascon solution can be used to improve the calibration of sea-level rise projections from numerical ice sheet models. Previous studies on ice sheet projections have used discrepancies between modeled and observed regional mass change trends in a Bayesian framework to calibrate uncertainties (Edwards et al., 2019; Nias et al., 2019; Ruckert et al., 2017; Ritz et al., 2015). The GSFC high-resolution mass change trend product will allow refinement of these calibrations by evaluating whether the numerical ice sheet models are able to reproduce the observed mass change trends at a finer spatial scale. In other words, whereas before the models were evaluated based on their ability to reproduce observed mass changes over regional spatial scales, our product will allow models to be evaluated based on their ability to reproduce the more localized changes that we observe.

Appendix A: Least-Squares Estimation Procedures

Before developing the regression model mascon estimation procedure, we first present the estimation of a global set of static mascon equivalent-water-height (EWH) values comprising the vector \mathbf{x} . These mascons are tiles of a thin layer covering the ellipsoidal Earth surface such that the j th mascon is nonzero over colatitude range $\left[\theta_j - \frac{\Delta\theta}{2}, \theta_j + \frac{\Delta\theta}{2}\right]$ and longitude range $\left[\phi_j - \frac{\Delta\phi}{2}, \phi_j + \frac{\Delta\phi}{2}\right]$, and whose mass is equivalent to a water-filled volume equal to the product of this area and the j th mascon EWH in units of cm, x_j . These x_j are related to a set of spherical harmonic (SH) coefficients through (Wahr et al., 1998)

$$c_\ell^m = \frac{10(1 + k_\ell)}{(2\ell + 1)M} \sum_{j=1}^{N_s} x_j r_j^2 \left(\frac{r_j}{a}\right)^\ell \int_{\phi_j - \frac{\Delta\phi}{2}}^{\phi_j + \frac{\Delta\phi}{2}} \int_{\theta_j - \frac{\Delta\theta}{2}}^{\theta_j + \frac{\Delta\theta}{2}} Y_\ell^m(\theta, \phi) \sin\theta \, d\theta \, d\phi, \quad (\text{A1})$$

where ℓ and m are SHC degree and order, respectively, M is the mass of the Earth, k_ℓ is the load Love number of degree ℓ , N_s is the number of mascon tiles covering the globe, r_j is the radius of mascon x_j following the ellipsoid, a is the equatorial radius of the Earth, and Y_ℓ^m is the normalized spherical harmonic function of degree ℓ and order m . Equation A1 may be expressed in matrix-vector form as

$$\mathbf{c} = \mathbf{L}\mathbf{x}, \quad (\text{A2})$$

where

$$L_{ij} = \frac{10(1 + k_{\ell_i})r_j^2}{(2\ell_i + 1)M} \left(\frac{r_j}{a}\right)^{\ell_i} \int_{\phi_j - \frac{\Delta\phi}{2}}^{\phi_j + \frac{\Delta\phi}{2}} \int_{\theta_j - \frac{\Delta\theta}{2}}^{\theta_j + \frac{\Delta\theta}{2}} Y_{\ell_i}^{m_i}(\theta, \phi) \sin\theta \, d\theta \, d\phi, \quad (\text{A3})$$

where ℓ_i and m_i are the degree and order, respectively, of the SH coefficient $c_{\ell_i}^{m_i}$. We have computed the SH normal equations and components of \mathbf{L} up to degree and order 96.

We seek to estimate the mascon vector, $\tilde{\mathbf{x}}$, that minimizes the cost function

$$J(\mathbf{x}) = [\mathbf{d} - \mathbf{a}(\mathbf{c}(\mathbf{x}))]^T \mathbf{W}[\mathbf{d} - \mathbf{a}(\mathbf{c}(\mathbf{x}))] + \lambda \mathbf{x}^T \mathbf{P}\mathbf{x}, \quad (\text{A4})$$

where the first term is the weighted misfit between the data vector \mathbf{d} of inter-satellite range-rate measurements and the model prediction vector \mathbf{a} , which is a nonlinear function of \mathbf{c} and ultimately \mathbf{x} via equation. A.2, as prescribed by the data noise covariance matrix \mathbf{W}^{-1} , and the second term is the discrepancy between \mathbf{x} and the preferred mascon state, which is $\mathbf{0}$ in this case, as prescribed by the mascon signal covariance matrix $\lambda^{-1}\mathbf{P}^{-1}$. We employ the Gauss-Newton (GN) nonlinear least-squares estimator (Seber & Wild, 2003) to obtain $\tilde{\mathbf{x}}$ where the k th step update is given as

$$\text{GN}_k \begin{cases} \tilde{\mathbf{c}}_k &= \mathbf{L}\tilde{\mathbf{x}}_k, \\ \mathbf{N} &= \mathbf{A}^T\mathbf{W}\mathbf{A}, \\ \Delta\tilde{\mathbf{c}}_k &= \mathbf{N}^{-1}\mathbf{A}^T\mathbf{W}(\mathbf{d} - \mathbf{a}(\tilde{\mathbf{c}}_k)), \\ \tilde{\mathbf{c}}_{k+1} &= \tilde{\mathbf{c}}_k + \Delta\tilde{\mathbf{c}}_k, \\ \tilde{\mathbf{x}}_{k+1} &= \mathbf{P}^{-1}\mathbf{L}^T(\lambda\mathbf{N}^{-1} + \mathbf{L}\mathbf{P}^{-1}\mathbf{L}^T)^{-1}\tilde{\mathbf{c}}_{k+1}, \end{cases} \quad (\text{A5})$$

where \mathbf{A} is the Jacobian matrix of $\mathbf{a}(\tilde{\mathbf{c}}_k)$. Equations similar to those in Equation. A5 are presented in (Sabaka et al., 2010) where they are discussed in the context of Optimal Filtering (Klees et al., 2008) and are termed an Anisotropic, Non-Symmetric (ANS) filter. These are also related to a two-step Least-Squares Collocation (LSC) (Moritz, 1980) process in which a SH signal auto-covariance, $\lambda^{-1}\mathbf{L}\mathbf{P}^{-1}\mathbf{L}^T$, and a SH noise covariance, \mathbf{N}^{-1} , map the raw $\tilde{\mathbf{c}}_{k+1}$ of Equation. A5 into filtered SH coefficients followed by a filter prediction into mascon space via a mascon-SH signal cross-covariance, $\lambda^{-1}\mathbf{P}^{-1}\mathbf{L}^T$.

We now extend these equations for the estimation of regression model mascon EWHs that are not static, but rather are time dependent such that the temporal behavior of x_j is described as

$$x_j(t) = \mathbf{f}^T(t)\mathcal{X}_j, \quad (\text{A6})$$

where \mathbf{f} is a vector of temporal basis functions and \mathcal{X}_j is a set of corresponding multipliers for the j th mascon EWH. In the case where a bias, trend, and sinusoid at a particular angular frequency, ω , describe the temporal variation of the mascons, then

$$\mathbf{f} = \begin{pmatrix} 1 \\ t \\ \cos \omega t \\ \sin \omega t \end{pmatrix}, \quad \mathcal{X}_j = \begin{pmatrix} x_{b_j} \\ x_{t_j} \\ x_{c_j} \\ x_{s_j} \end{pmatrix}, \quad (\text{A7})$$

where t is the elapsed time from some epoch (we use 2008.0), and the set of bias x_{b_j} , trend x_{t_j} , cosine x_{c_j} , and sine x_{s_j} multipliers for every j th mascon comprise the regression mascon vector

$$\mathbf{x}_{\text{reg}} = \begin{pmatrix} \mathcal{X}_1 \\ \vdots \\ \mathcal{X}_{N_s} \end{pmatrix}. \quad (\text{A8})$$

It should also be noted that the i th time-dependent SH coefficient $c_i(t)$ has the same temporal structure as the mascons. It is then straight forward to modify equation. A5 to accommodate the temporal multipliers of each mascon EWH.

It should be clear that the dimension of our estimated parameter vector, $\tilde{\mathbf{x}}_{\text{reg}}$, is equal to N_s multiplied by the number of temporal functions contained in \mathbf{f} . For the work presented here, N_s is equal to 41,168 and the regression model has four terms, resulting in a total of 164,672 parameters in $\tilde{\mathbf{x}}_{\text{reg}}$, and the corresponding regression regularization matrix, \mathbf{P}_{reg} , has dimensions $164,672 \times 164,672$. As discussed in the main text, our monthly mascon estimation procedure applies a block-diagonal structure in the regularization matrix for the mitigation of signal leakage across constraint region boundaries, but we observe that a diagonal regularization matrix is more appropriate for the high-resolution regression mascons due to the significant increase in spatial coverage that results from utilizing many years of Level 1B data. The simplicity of the diagonal regularization is less invasive in the sense that individual mascons may be treated as independent stochastic signals rather than linear combinations in the block-diagonal formulation, thus enforcing less, possibly artificial, structure than the data may indicate for a given

regularization strength. The diagonal terms of \mathbf{P}_{reg} are defined as $1/\sigma_{q_j}^2$, where the subscript q refers to the component of \mathcal{X}_j (b , t , c , s) and $\sigma_{q_j}^2$ is the assigned signal variance of a particular component of \mathbf{x}_{reg} . For example, $\sigma_{t_j}^2$ defines the assigned signal variance of the trend for the j th mascon, x_{t_j} . We tested a number of regularization design strategies and found that the most effective approach defined the σ values from the lower resolution (i.e., monthly) regression model fits for each mascon and temporal component. In order to not overly influence the high-resolution solution with the low-resolution solution via the applied regularization, we apply a simple approach to limit the σ magnitudes of the largest values. To implement this, the trend sigma for the j th mascon is defined as:

$$\sigma_{t_j} = \frac{|\tilde{\beta}_{t_j}|}{\exp(|\tilde{\beta}_{t_j}|/\max(|\tilde{\beta}_{t_j}|))}, \quad (\text{A9})$$

where $\tilde{\beta}_{t_j}$ is the low-resolution trend fit for the j th mascon. The same approach is applied to the bias and periodic terms contained in \mathbf{x}_{reg} and defined by \mathbf{f} in Equation A.7. Regarding the regularization parameter, λ , we note that it has been common for GRACE mascon estimation to select the smallest value possible before the non-geophysical stripes emerge in the solution (Loomis, Luthcke, & Sabaka, 2019; Watkins et al., 2015). For the high-resolution trends, we observe that following this general approach leads to a regularization parameter that also optimizes the agreement with the GOCO-06S solution.

Appendix B: GIA Models and Uncertainties

In order to provide a consistent comparison, we apply the same GIA correction to the GRACE/GFO trend estimates as was applied when deriving the ICESat/ICESat-2 estimates in Smith et al. (2020). The full set of GIA models and rheologies used to compute the applied correction are listed in Table B1. The GrIS GIA correction is defined as the mean of SM09 and ICE-6G_D (where SM09 is defined as the mean of the nine different SM09 rheologies). The AIS correction is defined as the mean of IJ05-R2, W12a, and ICE-6G_D (where again IJ05-R2 and W12a are defined by the mean of the rheologies listed). Figure B1 shows the ICE-6G_D and Smith et al. (2020) GIA models and their differences over the ice sheets. We define the uncertainties as twice the standard deviation of the full suite of models listed in Table B1 for each region (10 models for GrIS and 9 models for AIS). We note that our final AIS GIA correction of $56 \pm 26 \text{ Gt yr}^{-1}$ encompasses the expected value of 74 Gt yr^{-1} reported in the recent statistical analysis of AIS GIA corrections presented by Caron and Ivins (2020). We applied the ICE-6G_D correction for all global analyses, as that model is currently widely used for GRACE/GFO and is readily available, as opposed to the model of Smith et al. (2020) that needs to be constructed as described above.

Data Availability Statement

The NASA GSFC monthly and high-resolution trend mascon products are available at <https://earth.gsfc.nasa.gov/geo/data/grace-mascons>. All GRACE and GRACE-FO products and Technical Notes are available at <https://podaac-tools.jpl.nasa.gov/drive/files/allData>. The DDK5 filtered solutions are available at http://icgem.gfz-potsdam.de/series/01_GRACE/CSR/. The ICE-6G_D GIA model is provided in the (R. W. Peltier et al., 2018) Sup-

Table B1
GIA Model Parameters for ICE-6G_D (R. W. Peltier et al., 2018), SM09 (Simpson et al., 2009), IJ05-R2 (Ivins et al., 2013), and W12a (Whitehouse et al., 2012)

Model	Region	Lithospheric	Upper mantle	Lower mantle
		thickness	viscosity	viscosity
		[km]	[$10^{21} \text{ Pa}\cdot\text{s}$]	[$10^{21} \text{ Pa}\cdot\text{s}$]
ICE-6G_D	GrIS & AIS	10 ^a	0.5	1.5–3.2 ^b
SM09	GrIS	96	0.3	2.0
SM09	GrIS	96	0.5	10.0
SM09	GrIS	96	0.5	5.0
SM09	GrIS	96	0.5	8.0
SM09	GrIS	96	0.8	5.0

Table B1
Continued

Model	Region	Lithospheric	Upper mantle	Lower mantle
		thickness	viscosity	viscosity
		[km]	[10^{21} Pa·s]	[10^{21} Pa·s]
SM09	GrIS	120	0.1	1.0
SM09	GrIS	120	0.5	1.0
SM09	GrIS	120	0.5	3.0
SM09	GrIS	120	0.8	1.0
IJ05-R2	AIS	65	0.2	1.5
IJ05-R2	AIS	115	0.2	1.5
IJ05-R2	AIS	115	0.2	2.0
IJ05-R2	AIS	115	0.2	3.2
IJ05-R2	AIS	115	0.2	4.0
W12a	AIS	96	0.8	20.0
W12a	AIS	120	1.0	5.0
W12a	AIS	120	1.0	10.0

^aElastic layer for 0-60 km and viscosity 10^{22} Pa·s for 60-100 km (W. R. Peltier et al., 2015). ^b 1.5×10^{21} Pa·s for 670-1260 km and 3.2×10^{21} Pa·s for 1260-2890 km (W. R. Peltier et al., 2015).

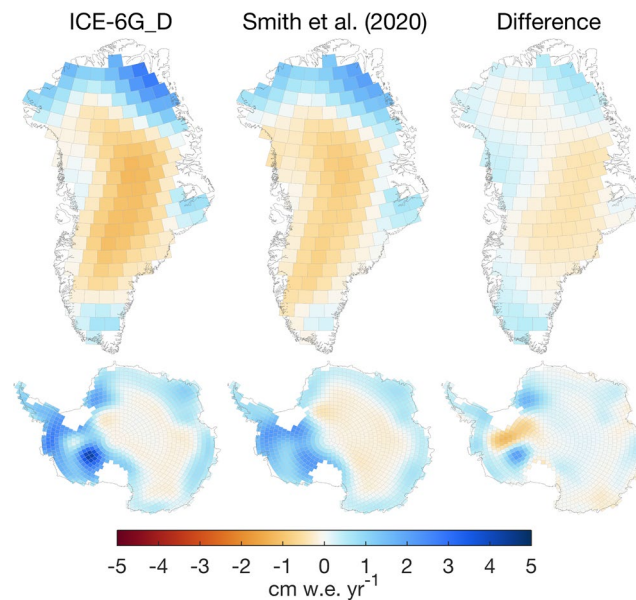


Figure B1. GIA models for the Greenland and Antarctic Ice Sheet mascons: ICE-6G_D (R. W. Peltier et al., 2018), Smith et al. (2020), and the difference (ICE-6G_D – Smith).

porting Information. The (Smith et al., 2020) mass change grids are available at <https://digital.lib.washington.edu/researchworks/handle/1773/45388>.

References

- Bolch, T., Sandberg Srensen, L., Simonsen, S. B., Mlg, N., Machguth, H., Rastner, P., & Paul, F. (2013). Mass loss of Greenland's glaciers and ice caps 2003?2008 revealed from ICESat laser altimetry data. *Geophysical Research Letters*, 40(5), 875–881. <https://doi.org/10.1002/grl.50270>. Retrieved from <https://agupubs.onlinelibrary.wiley.com/doi/abs/10.1002/grl.50270>
- Caron, L., & Ivins, E. R. (2020). A baseline antarctic gia correction for space gravimetry. *Earth and Planetary Science Letters*, 531, 115957. <https://doi.org/10.1016/j.epsl.2019.115957>. Retrieved from <https://www.sciencedirect.com/science/article/pii/S0012821X19306491>

Acknowledgments

This work was funded by the NASA GRACE-FO Science Team, NN-H19ZDA001N-GRACEFO and the NASA Sea Level Change Team, NN-H19ZDA001N-SLCST. We acknowledge the important contributions to the GRACE data processing system by our colleagues Kenneth Rachlin, Dave Rowlands, and Joseph Nicholas, and useful discussions with Michael Croteau. We are grateful for the useful comments provided by the editor and reviewers.

- Colgan, W., Abdalati, W., Citterio, M., Csatho, B., Fettweis, X., Luthcke, S., & Stober, M. (2015). Hybrid glacier Inventory, Gravimetry and Altimetry (HIGA) mass balance product for Greenland and the Canadian Arctic. *Remote Sensing of Environment*, *168*, 24–39. <https://doi.org/10.1016/j.rse.2015.06.016>. Retrieved from <https://www.sciencedirect.com/science/article/pii/S0034425715300468>
- Croteau, M. J., Sabaka, T. J., & Loomis, B. D. (2021). Grace fast mascons from spherical harmonics and a regularization design trade study. *Journal of Geophysical Research: Solid Earth*, *126*(8), e2021JB022113. <https://doi.org/10.1029/2021JB022113>. Retrieved from <https://agupubs.onlinelibrary.wiley.com/doi/abs/10.1029/2021JB022113>
- Csatho, B. M., Schenk, A. F., van der Veen, C. J., Babonis, G., Duncan, K., Rezvanbehbahani, S., & van Angelen, J. H. (2014). Laser altimetry reveals complex pattern of greenland ice sheet dynamics. *Proceedings of the National Academy of Sciences*, *111*(52), 18478–18483. <https://doi.org/10.1073/pnas.1411680112>. Retrieved from <https://www.pnas.org/content/111/52/18478>
- Dobslaw, H., Bergmann-Wolf, I., Dill, R., Poropat, L., & Flechtner, F. (2017). *Product Description Document for AOD1B Release 06*. Retrieved from https://podaac-tools.jpl.nasa.gov/drive/files/allData/gracefo/docs/AOD1B_PDD_RL06_v6.1.pdf (GRACE Project Document 327–750).
- Edwards, T. L., Brandon, M. A., Durand, G., Edwards, N. R., Golledge, N. R., Holden, P. B., & Wernecke, A. (2019). Revisiting antarctic ice loss due to marine ice-cliff instability. *Nature*, *566*, 58–64. <https://doi.org/10.1038/s41586-019-0901-4>
- Elsaka, B., Raimondo, J.-C., Brieden, P., Reubelt, T., Kusche, J., Flechtner, F., & Müller, J. (2014). Comparing seven candidate mission configurations for temporal gravity field retrieval through full-scale numerical simulation. *Journal of Geodesy*, *88*(1), 31–43. <https://doi.org/10.1007/s00190-013-0665-9>
- Gardner, A. S., Moholdt, G., Cogley, J. G., Wouters, B., Arendt, A. A., Wahr, J., & Paul, F. (2013). A Reconciled Estimate of Glacier Contributions to Sea Level Rise: 2003 to 2009. *Science*, *340*(6134), 852–857. <https://doi.org/10.1126/science.1234532>. Retrieved from <https://science.sciencemag.org/content/340/6134/852>
- Han, S., Riva, R., Sauber, J., & Okal, E. (2013). Source parameter inversion for recent great earthquakes from a decade-long observation of global gravity fields. *Journal of Geophysical Research: Solid Earth*, *118*(3), 1240–1267. <https://doi.org/10.1002/jgrb.50116>
- Ivins, E. R., James, T. S., Wahr, J., Schrama, O., E. J., Landerer, F. W., & Simon, K. M. (2013). Antarctic contribution to sea level rise observed by grace with improved gia correction. *Journal of Geophysical Research: Solid Earth*, *118*(6), 3126–3141. <https://doi.org/10.1002/jgrb.50208>. Retrieved from <https://agupubs.onlinelibrary.wiley.com/doi/abs/10.1002/jgrb.50208>
- Jacob, T., Wahr, J., Pfeffer, W., & Swenson, S. (2012). Recent contributions of glaciers and ice caps to sea level rise. *Nature*, *482*, 514–518. Retrieved from <https://doi.org/10.1038/nature10847>
- Joughin, I., Tulaczyk, S., Bindschadler, R., & Price, S. F. (2002). Changes in west Antarctic ice stream velocities: Observation and analysis. EPM 3-1-EPM 3-22. *Journal of Geophysical Research: Solid Earth*, *107*(B11). <https://doi.org/10.1029/2001jb001029>. Retrieved from <https://agupubs.onlinelibrary.wiley.com/doi/abs/10.1029/2001JB001029>
- Klees, R., Revtova, E. A., Gunter, B. C., Ditmar, P., Oudman, E., Winsemius, H. C., & Savenije, H. H. G. (2008). The design of an optimal filter for monthly GRACE gravity models. *Geophysical Journal International*, *175*(2), 417–432. <https://doi.org/10.1111/j.1365-246X.2008.03922.x>
- Kusche, J., Schmidt, R., Petrovic, S., & Rietbroek, R. (2009, 10). Decorrelated GRACE time-variable gravity solutions by GFZ, and their validation using a hydrological model. *Journal of Geodesy*, *83*(10), 903–913. <https://doi.org/10.1007/s00190-009-0308-3>
- Kvas, A., Brockmann, J. M., Krauss, S., Schubert, T., Gruber, T., & Meyer, U., Pail, R. (2020). GOCO06s - A satellite-only global gravity field model. *Earth System Science Data Discussions*. <https://doi.org/10.5194/essd-2020-192>
- Landerer, F. W., Flechtner, F. M., Save, H., Webb, F. H., Bandikova, T., Bertiger, W. I., & Yuan, D.-N. (2020). Extending the global mass change data record: Grace follow-on instrument and science data performance. *Geophysical Research Letters*, *47*(12), e2020GL088306. <https://doi.org/10.1029/2020GL088306>. Retrieved from <https://agupubs.onlinelibrary.wiley.com/doi/abs/10.1029/2020GL088306>
- Li, X., Rignot, E., Morlighem, M., Mouginot, J., & Scheuchl, B. (2015). Grounding line retreat of Totten Glacier, East Antarctica, 1996 to 2013. *Geophysical Research Letters*, *42*(19), 8049–8056. <https://doi.org/10.1002/2015GL065701>. Retrieved from <https://agupubs.onlinelibrary.wiley.com/doi/abs/10.1002/2015GL065701>
- Loomis, B. D., Luthcke, S. B., & Sabaka, T. J. (2019). Regularization and error characterization of GRACE mascons. *Journal of Geodesy*, *93*, 1381–1398. <https://doi.org/10.1007/s00190-019-01252-y>
- Loomis, B. D., Rachlin, K. E., & Luthcke, S. B. (2019). Improved Earth oblateness rate reveals increased ice sheet losses and mass-driven sea level rise. *Geophysical Research Letters*, *46*, 6910–6917. <https://doi.org/10.1029/2019gl082929>
- Loomis, B. D., Rachlin, K. E., Wiese, D. N., Landerer, F. W., & Luthcke, S. B. (2020). Replacing GRACE/GRACE-FO With Satellite Laser Ranging: Impacts on Antarctic Ice Sheet Mass Change. *Geophysical Research Letters*, *47*(3), e2019GL085488. <https://doi.org/10.1029/2019GL085488>. Retrieved from <https://agupubs.onlinelibrary.wiley.com/doi/abs/10.1029/2019GL085488>
- Loomis, B. D., Richey, A. S., Arendt, A. A., Appana, R., Deweese, Y.-J. C., Forman, B. A., & Shean, D. E. (2019). Water Storage Trends in High Mountain Asia. *Frontiers in Earth Science*, *7*, 235. <https://doi.org/10.3389/feart.2019.00235>. Retrieved from <https://www.frontiersin.org/article/10.3389/feart.2019.00235>
- Luthcke, S. B., Sabaka, T., Loomis, B., Arendt, A., McCarthy, J., & Camp, J. (2013). Antarctica, Greenland and Gulf of Alaska land-ice evolution from an iterated GRACE global mascon solution. *Journal of Glaciology*, *59*(216), 613–631. <https://doi.org/10.3189/2013JoG12J147>
- Moritz, H. (1980). *Advanced physical geodesy*. Abacus.
- Mouginot, J., Rignot, E., Björk, A. A., van den Broeke, M., Millan, R., Morlighem, M., & Wood, M. (2019). Forty-six years of Greenland Ice Sheet mass balance from 1972 to 2018. *Proceedings of the National Academy of Sciences*, *116*(19), 9239–9244. <https://doi.org/10.1073/pnas.1904242116>. Retrieved from <https://www.pnas.org/content/116/19/9239>
- Mouginot, J., Rignot, E., & Scheuchl, B. (2014). Sustained increase in ice discharge from the Amundsen Sea Embayment, West Antarctica, from 1973 to 2013. *Geophysical Research Letters*, *41*(5), 1576–1584. <https://doi.org/10.1002/2013GL059069>. Retrieved from <https://agupubs.onlinelibrary.wiley.com/doi/abs/10.1002/2013GL059069>
- Nias, I. J., Cornford, S. L., Edwards, T. L., Gourmelen, N., & Payne, A. J. (2019). Assessing Uncertainty in the Dynamical Ice Response to Ocean Warming in the Amundsen Sea Embayment, West Antarctica. *Geophysical Research Letters*, *46*(20), 11253–11260. <https://doi.org/10.1029/2019GL084941>. Retrieved from <https://agupubs.onlinelibrary.wiley.com/doi/abs/10.1029/2019GL084941>
- Noël, B., van de Berg, W. J., Lhermitte, S., Wouters, B., Machguth, H., Howat, I., & van den Broeke, M. R. (2017). A tipping point in re-freezing accelerates mass loss of Greenland’s glaciers and ice caps. *Nature Communications*, *8*(1). Retrieved from <https://doi.org/10.1038/ncomms14730>
- Peltier, R. W., Argus, D. F., & Drummond, R. (2018). Comment on “An Assessment of the ICE-6G_C (VM5a) Glacial Isostatic Adjustment Model” by Purcell et al. *Journal of Geophysical Research: Solid Earth*, *123*(2), 2019–2028. <https://doi.org/10.1002/2016JB013844>. Retrieved from <https://agupubs.onlinelibrary.wiley.com/doi/abs/10.1002/2016JB013844>
- Peltier, W. R., Argus, D. F., & Drummond, R. (2015). Space geodesy constrains ice age terminal deglaciation: The global ICE-6G_C (VM5a) model. *Journal of Geophysical Research: Solid Earth*, *120*(1), 450–487. <https://doi.org/10.1002/2014jb011176>. Retrieved from <https://agupubs.onlinelibrary.wiley.com/doi/abs/10.1002/2014JB011176>

- Rignot, E., Mouginot, J., Scheuchl, B., van den Broeke, M., van Wessel, M. J., & Morlighem, M. (2019). Four decades of antarctic ice sheet mass balance from 1979–2017. *Proceedings of the National Academy of Sciences*, *116*(4), 1095–1103. <https://doi.org/10.1073/pnas.1812883116>. Retrieved from <https://www.pnas.org/content/116/4/1095>
- Ritz, C., Edwards, T. L., Durand, G., Payne, A. J., Peyaud, V., & Hindmarsh, R. C. A. (2015). Potential sea-level rise from Antarctic ice-sheet instability constrained by observations. *Nature*, *528*, 115–118. Retrieved from <https://doi.org/10.1038/nature16147>
- Rodell, M., Famiglietti, J. S., Wiese, D. N., Reager, J. T., Beadoing, H. K., Landerer, F. W., & Lo, M.-H. (2018). Emerging trends in global freshwater availability. *Nature*, *557*, 651–659. Retrieved from <https://doi.org/10.1038/s41586-018-0123-1>
- Ruckert, K. L., Shaffer, G., Pollard, D., Guan, Y., Wong, T. E., Forest, C., & Keller, K. (2017). Assessing the Impact of Retreat Mechanisms in a Simple Antarctic Ice Sheet Model Using Bayesian Calibration. *PLoS ONE*, *12*(1), e0170052. Retrieved from <https://doi.org/10.1371/journal.pone.0170052>
- Sabaka, T. J., Rowlands, D. D., Luthcke, S. B., & Boy, J.-P. (2010). Improving global mass flux solutions from Gravity Recovery and Climate Experiment (GRACE) through forward modeling and continuous time correlation. *Journal of Geophysical Research: Solid Earth*, *115*(B11). <https://doi.org/10.1029/2010JB007533>
- Save, H., Bettadpur, S., & Tapley, B. D. (2016). High-resolution csr grace r105 mascons. *Journal of Geophysical Research: Solid Earth*, *121*(10), 7547–7569. <https://doi.org/10.1002/2016JB013007>. Retrieved from <https://agupubs.onlinelibrary.wiley.com/doi/abs/10.1002/2016JB013007>
- Scanlon, B. R., Zhang, Z., Save, H., Sun, A. Y., Müller Schmied, H., van Beek, L. P. H., & Bierkens, M. F. P. (2018). Global models underestimate large decadal declining and rising water storage trends relative to GRACE satellite data. *Proceedings of the National Academy of Sciences*, *115*(6), E1080–E1089. <https://doi.org/10.1073/pnas.1704665115>. Retrieved from <https://www.pnas.org/content/115/6/E1080>
- Seber, G. A. F., & Wild, C. J. (2003). *Nonlinear Regression*. Wiley-Interscience.
- Simpson, M. J., Milne, G. A., Huybrechts, P., & Long, A. J. (2009). Calibrating a glaciological model of the Greenland ice sheet from the Last Glacial Maximum to present-day using field observations of relative sea level and ice extent. *Quaternary Science Reviews*, *28*(17), 1631–1657. <https://doi.org/10.1016/j.quascirev.2009.03.004>. Retrieved from <https://www.sciencedirect.com/science/article/pii/S0277379109000997> (Quaternary Ice Sheet-Ocean Interactions and Landscape Responses).
- Smith, B., Fricker, H. A., Gardner, A. S., Medley, B., Nilsson, J., Paolo, F. S., & Zwally, H. J. (2020). Pervasive ice sheet mass loss reflects competing ocean and atmosphere processes. *Science*, *368*(6496), 1239–1242. <https://doi.org/10.1126/science.aaz5845>. Retrieved from <https://science.sciencemag.org/content/368/6496/1239>
- Sun, Y., Riva, R., & Ditmar, P. (2016). Optimizing estimates of annual variations and trends in geocenter motion and J2 from a combination of GRACE data and geophysical models. *Journal of Geophysical Research: Solid Earth*, *121*(11), 8352–8370. <https://doi.org/10.1002/2016JB013073>. Retrieved from <https://agupubs.onlinelibrary.wiley.com/doi/abs/10.1002/2016JB013073>
- Sutterley, T. C., Velicogna, I., Rignot, E., Mouginot, J., Flament, T., van den Broeke, M. R., & Reijmer, C. H. (2014). Mass loss of the amundsen sea embayment of west antarctica from four independent techniques. *Geophysical Research Letters*, *41*(23), 8421–8428. <https://doi.org/10.1002/2014GL061940>. Retrieved from <https://agupubs.onlinelibrary.wiley.com/doi/abs/10.1002/2014GL061940>
- Velicogna, I., Mohajerani, Y., AG., Landerer, F., Mouginot, J., Noel, B., et al. (2020). Continuity of ice sheet mass loss in greenland and antarctica from the grace and grace follow-on missions. *Geophysical Research Letters*, *47*(8), e2020GL087291. <https://doi.org/10.1029/2020GL087291>. Retrieved from <https://agupubs.onlinelibrary.wiley.com/doi/abs/10.1029/2020GL087291>
- Wahr, J., Molenaar, M., & Bryan, F. (1998). Time variability of the earth's gravity field: Hydrological and oceanic effects and their possible detection using grace. *Journal of Geophysical Research: Solid Earth*, *103*(B12), 30205–30229. <https://doi.org/10.1029/98JB02844>. Retrieved from <https://agupubs.onlinelibrary.wiley.com/doi/abs/10.1029/98JB02844>
- Watkins, M. M., Wiese, D. N., Yuan, D.-N., Boening, C., & Landerer, F. W. (2015). Improved methods for observing Earth's time variable mass distribution with GRACE using spherical cap mascons. *Journal of Geophysical Research: Solid Earth*, *120*(4), 2648–2671. <https://doi.org/10.1002/2014JB011547>. Retrieved from <https://agupubs.onlinelibrary.wiley.com/doi/abs/10.1002/2014JB011547>
- Whitehouse, P. L., Bentley, M. J., Milne, G. A., King, M. A., & Thomas, I. D. (2012). A new glacial isostatic adjustment model for Antarctica: calibrated and tested using observations of relative sea-level change and present-day uplift rates. *Geophysical Journal International*, *190*(3), 1464–1482. <https://doi.org/10.1111/j.1365-246X.2012.05557.x>
- Zwally, H. J., Li, J., Robbins, J. W., Saba, J. L., Yi, D., & Brenner, A. C. (2015). Mass gains of the Antarctic ice sheet exceed losses. *Journal of Glaciology*, *61*(230), 1019–1036. <https://doi.org/10.3189/2015JG15J071>. Retrieved from <https://www.cambridge.org/core/journals/journal-of-glaciology/article/mass-gains-of-the-antarctic-ice-sheet-exceed-losses/983F196E23C3A6E7908E5FB32EB42268>